ATLAS CONF Note
ATLAS-CONF-2019-056
13th November 2019

Measurement of suppression of large-radius jets and its dependence on substructure in Pb+Pb at 5.02 TeV with the ATLAS detector

The ATLAS Collaboration

This note presents measurement of the nuclear modification factor of large-radius jets in $\sqrt{s_{\mathrm{NN}}} = 5.02$ TeV Pb+Pb collisions by the ATLAS experiment. The measurement is performed using 1.72 nb^{-1} and 257 pb^{-1}of Pb+Pb and pp data, respectively. The large-radius jets are reconstructed with the anti-k_t algorithm using a radius parameter of $R = 1.0$, by re-clustering anti-k_t $R = 0.2$ jets having transverse momenta, $p_{\mathrm{T}} > 35$ GeV. After applying a trimming procedure, the large-radius jet constituents are re-clustered using the k_t algorithm in order to obtain the splitting parameter, $\sqrt{d_{12}}$, which characterizes the transverse momentum scale for the hardest splitting in the jet. The yield of the $R = 1.0$ jets is measured as a function of p_{T} and $\sqrt{d_{12}}$ over the rapidity and transverse momentum ranges, $|y| < 2$ and $156 < p_{\mathrm{T}} < 1000$ GeV, respectively. The nuclear modification factor, R_{AA}, obtained by comparing the Pb+Pb jet yields to those in pp collisions, is measured as a function of jet transverse momentum and $\sqrt{d_{12}}$. A significant evolution of R_{AA} with $\sqrt{d_{12}}$ is observed at small $\sqrt{d_{12}}$ values, indicating a significant difference in the quenching of large-radius jets having single sub-jet and those with more complex substructure. The inclusive jet R_{AA}, integrated over $\sqrt{d_{12}}$, is qualitatively similar to that obtained in previous measurements for $R = 0.4$ jets.

1 Introduction

Heavy-ion collisions at high energies are performed in order to produce and study hot, strongly-interacting matter often referred to as quark-gluon plasma (QGP) [1–4]. Hard-scattering processes that take place during the initial stages of the nuclear collisions produce high-energy quarks and gluons that subsequently lose their energy through interactions with the plasma. The fragmentation of high-transverse momentum (p_{T}) quarks and gluons results in groups of angularly-correlated hadrons, referred to as jets, whose momenta and structure can also be modified at momenta and structure level by the energy-loss process. Measurements of the yield and properties of jets can provide insight into the energy-loss process and, ultimately, the properties of the QGP itself.

The ATLAS Collaboration measured correlated production of nearby jets in Pb+Pb collisions at 2.76 TeV, reporting centrality dependent suppression of the conditional neighbouring jet yields with respect to yields in pp collisions [5]. Recently, the ATLAS Collaboration published a measurement of the yields of charged particles associated with anti-k_t jets with radius parameter $R = 0.4$ up to an angular distance of $\Delta R = 0.8$ from the jet axis showing jet broadening for low transverse momentum (p_{T}) particles inside the jet in central Pb+Pb collisions compared to those in pp collisions. In contrast, for higher-p_{T} particles, the angular distributions were found to be narrower in Pb+Pb collisions than in pp collisions [6]. This observation suggests a dependence of modification of production of jets based on their internal structure and modification of production of neighboring jets. This measurement allows also an interpretation in which jets having large-angle hard splittings could be more suppressed relative to those with small-angle or only soft splittings. A similar observation was obtained by the CMS Collaboration using a different approach [7]. Such behavior is predicted [8–11] in descriptions of jet quenching where coherent parton branching plays a role. In this picture, the medium can only resolve partonic fragments at a certain transverse resolution scale below which they act coherently as a single emitter.

The ATLAS Collaboration has also presented a preliminary measurement of jet suppression in Pb+Pb collisions evaluated as a function of m/p_{T} for $R = 0.4$ jets, where m represents the jet mass [12]. This measurement could be sensitive to color coherence/decoherence effects. The R_{AA} values showed an overall suppression of jet yields compatible with the inclusive study without significant dependence on m/p_{T}. The precision of that measurement was limited due to larger systematical uncertainties. A similar measurement was also performed by the ALICE Collaboration [13]. Furthermore, CMS Collaboration published a measurement of the per-jet normalized splitting function, z_g, in pp and Pb+Pb collisions where $R = 0.4$ jets are used which have soft wide-angle radiation removed using a soft-drop method [14]. A steeper distribution of z_g is observed with depletion of jets with higher z_g values in Pb+Pb collisions. However, these measurements are intrinsically limited by the small radii used for the jets since the jet size automatically limits the kinematics of the internal splitting that can be measured. Furthermore, measurement of yields is directly sensitive to the energy loss contrarily to per-jet normalized measurements.

To address the above-described limitations of previous measurements, ATLAS has measured jets in Pb+Pb collisions using a large radius, $R = 1.0$. The $R = 1.0$ jets are clustered from small-radius, $R = 0.2$, anti-k_t jets with $p_{\mathrm{T}} > 35$ GeV reconstructed using the standard ATLAS heavy-ion jet reconstruction algorithm described in Section 4. This procedure limits the impact of the underlying event (UE) on the measurement but also does not allow recovering the energy transferred outside the $R = 0.2$ sub-jets via jet quenching. Therefore, this measurement studies the hard parton splittings. The k_t jet finding algorithm [15] is used to re-cluster $R = 1.0$ jet constituents to obtain the k_t splitting scales. The splitting scales are determined by clustering objects together according to their distance from each other with the following distance definition:

$$d_{ij} = \min(p_{\mathrm{T,i}}^2, p_{\mathrm{T,j}}^2) \cdot \Delta R_{ij}^2, \quad \Delta R_{ij} = \sqrt{\Delta\phi_{ij}^2 + \Delta y_{ij}^2},$$

where input objects are labeled with an index corresponding to the i-th and j-th momentum in the list of inputs, for all possible permutations of i and j in the given clustering step. This note presents the measurement of the splitting scale $\sqrt{d_{12}}$ where indices 1 and 2 refer to the two jets before the final clustering step. For large-radius jets with only a single sub-jet, $\sqrt{d_{12}}$ is defined to be 0.

The jet yield measured in Pb+Pb collisions is compared to that measured in pp collisions using the nuclear modification factor, R_{AA}. R_{AA} is measured as a function of jet p_{T} and $\sqrt{d_{12}}$ in different Pb+Pb centrality intervals and is defined as

$$R_{\mathrm{AA}} = \frac{\left.\dfrac{1}{N_{\mathrm{evt}}} \dfrac{\mathrm{d}^3 N_{\mathrm{jet}}}{\mathrm{d}p_{\mathrm{T}}\mathrm{d}\sqrt{d_{12}}\mathrm{d}y}\right|_{\mathrm{cent}}}{\left.\langle T_{\mathrm{AA}}\rangle \dfrac{\mathrm{d}^3\sigma_{\mathrm{jet}}}{\mathrm{d}p_{\mathrm{T}}\mathrm{d}\sqrt{d_{12}}\mathrm{d}y}\right|_{pp}},$$

where N_{jet} and σ_{jet} are the jet yield in Pb+Pb collisions and the jet cross section in pp collisions, respectively, y is the jet rapidity[1], and N_{evt} is the total number of Pb+Pb collisions within a given centrality interval. $\langle T_{\mathrm{AA}}\rangle$ represents the mean nuclear thickness function that accounts for an enhancement of hard-scattering rate due to the larger geometric overlap between the colliding nuclei [16].

2 ATLAS detector

The measurements presented in this note are performed using the ATLAS calorimeter, inner detector, trigger, and data acquisition systems [17]. The calorimeter system consists of a sampling liquid-argon (LAr) electromagnetic (EM) calorimeter covering $|\eta| < 3.2$, a steel–scintillator sampling hadronic calorimeter covering $|\eta| < 1.7$, LAr hadronic calorimeters covering $1.5 < |\eta| < 3.2$, and two LAr forward calorimeters (FCal) covering $3.1 < |\eta| < 4.9$. The EM calorimeters are segmented longitudinally in shower depth into three layers with an additional pre-sampler layer. The hadronic calorimeters have three sampling layers longitudinal in shower depth in $|\eta| < 1.7$ and four sampling layers in $1.5 < |\eta| < 3.2$, with a slight overlap.

The inner detector measures charged particles within the pseudorapidity interval $|\eta| < 2.5$ using a combination of silicon pixel detectors, silicon microstrip detectors (SCT), and a straw-tube transition radiation tracker (TRT), all immersed in a 2 T axial magnetic field [17]. Each of the three detectors is composed of a barrel and two symmetric end-cap sections. The pixel detector is composed of four layers including the Insertable B-Layer [18, 19]. The SCT barrel section contains four layers of modules with sensors on both sides, and each end-cap consists of nine layers of double-sided modules with radial strips. The TRT contains layers of staggered straws interleaved with the transition radiation material.

---

[1] ATLAS uses a right-handed coordinate system with its origin at the nominal interaction point (IP) in the centre of the detector, and the z-axis along the beam pipe. The x-axis points from the IP to the centre of the LHC ring, and the y-axis points upward. Cylindrical coordinates (r, ϕ) are used in the transverse plane, ϕ being the azimuthal angle around the z-axis. The pseudorapidity is defined in terms of the polar angle θ as $\eta = -\ln\tan(\theta/2)$. The rapidity is defined as $y = 0.5\ln[(E + p_z)/(E - p_z)]$ where E and p_z are the energy and z-component of the momentum along the beam direction respectively. Transverse momentum and transverse energy are defined as $p_{\mathrm{T}} = p\sin\theta$ and $E_{\mathrm{T}} = E\sin\theta$, respectively. The angular distance between two objects with relative differences $\Delta\eta$ and $\Delta\phi$ in pseudorapidity and azimuth respectively is given by $\sqrt{(\Delta\eta)^2 + (\Delta\phi)^2}$.

The zero-degree calorimeters (ZDCs) are located symmetrically at $z = \pm 140$ m and cover $|\eta| > 8.3$. The ZDCs use tungsten plates as absorbers and quartz rods sandwiched between the tungsten plates as the active medium. In Pb+Pb collisions, the ZDCs primarily measure "spectator" neutrons that do not interact hadronically when the incident nuclei collide. A ZDC coincidence trigger is implemented by requiring the pulse height from both ZDCs to be above a threshold that is set to accept the signal corresponding to the energy deposition from a single neutron.

Events used in this analysis were selected by a two-level trigger system. The first, a hardware-based trigger stage named Level-1, is implemented with custom electronics. The next level is the software-based High-Level Trigger (HLT). The events were selected by the HLT, which was seeded by a L1 jet trigger performing a simple sliding window algorithm to find jet candidates and requiring minimum thresholds of 15, 20, and 30 GeV. The HLT jet triggers use a jet reconstruction algorithm similar to that used in the offline analysis and applies cuts on the minimum transverse energy, E_{T}, of $R = 0.4$ jets of 60, 75, and 85 GeV with exception of the highest-E_{T} trigger in pp collisions requiring a large-radius, $R = 1.0$, jet with $E_{\mathrm{T}} > 110$ GeV. The analysis is done in the region of jet p_{T} for which the triggers are fully efficient. In addition to the jet triggered sample, a minimum-bias (MB) triggered sample is used, which is defined by a logical OR of the following two triggers: a total energy Level-1 trigger of at least 50 GeV; a veto on the total-energy trigger, plus requirements of a ZDC coincidence trigger at Level-1 and at least one track in the HLT. More details about the jet triggering in heavy-ion collisions can be found in Ref. [20].

3 Event and data selection

This analysis utilizes 1.72 nb^{-1} of Pb+Pb data at $\sqrt{s_{\mathrm{NN}}} = 5.02$ TeV recorded in 2018 and 257 pb^{-1} of pp data collected in 2017 at the same collision energy. All events are required to have at least one reconstructed vertex, to have been collected during stable beam conditions, and to satisfy detector and data-quality requirements that include the detector subsystems being in nominal operating conditions. The number of inelastic interactions per bunch crossing is smaller than $3{\times}10^{-3}$ in Pb+Pb collisions, resulting in a small fraction of events ($< 0.5\%$) containing multiple collisions, know as "pileup". The anticorrelation between the total transverse energy deposited in the FCal, $\Sigma E_{\mathrm{T}}^{\mathrm{FCal}}$, and the number of neutrons detected in the ZDC is used to suppress these pileup events. Events with a much higher number of ZDC neutrons than the number expected from the bulk of events for a given value of $\Sigma E_{\mathrm{T}}^{\mathrm{FCal}}$ are rejected. The pp data were collected with the average number of inelastic interactions per bunch crossing ranging from 1.4 to 4.4. No pileup rejection is applied in the analysis of pp data.

In Pb+Pb collisions, the event centrality reflects the overlap area of the two colliding nuclei and is characterized by the $\Sigma E_{\mathrm{T}}^{\mathrm{FCal}}$ [21]. The five centrality intervals used in this analysis are defined according to successive percentiles of the $\Sigma E_{\mathrm{T}}^{\mathrm{FCal}}$ distribution obtained in MB collisions, ordered from the most central (highest $\Sigma E_{\mathrm{T}}^{\mathrm{FCal}}$) to the most peripheral (lowest $\Sigma E_{\mathrm{T}}^{\mathrm{FCal}}$) collisions: 0–10%, 10–20%, 20–40%, 40–60%, and 60–80%. The values of the mean nuclear thickness function, $\langle T_{\mathrm{AA}} \rangle$, and the number of nucleons participating in the collision, N_{part}, in each centrality interval are evaluated by a Glauber model analysis of the $\Sigma E_{\mathrm{T}}^{\mathrm{FCal}}$ distribution and tabulated in Ref. [5]. The total number of minimum-bias events in the centrality interval of 0-80%, that are used to estimate the per-event yields, corresponds to 10.2 billion.

This analysis uses several Monte Carlo (MC) samples to evaluate the performance of the detector and analysis procedure, and to correct the measured distributions for detector effects. The pp MC used in this analysis includes 32×10^6 Pythia8 [22] pp jet events at $\sqrt{s} = 5.02$ TeV with the A14 ATLAS tune [23] and the NNPDF23LO parton distribution functions [24]. Pileup from additional pp collisions is generated by Pythia8, with parameter values set to the A2 tune [25] and using the MSTW2008 [26] PDF set, with a distribution of the number of extra collisions matching that of data.

The Pb+Pb MC sample uses 32×10^6 pp Pythia8 events with the same tune and PDFs as in pp MC samples that are overlayed on top of events from a dedicated sample of Pb+Pb data events. This sample was recorded with combination of MB trigger and total energy triggers requiring 1.5 TeV or 6.5 TeV to enhance the number of central collisions. This "MC overlay" sample was reweighted on an event-by-event basis such that it has the same centrality distribution as the jet-triggered data sample. The detector response in all MC samples was simulated using Geant4 [27, 28].

4 Jet reconstruction and analysis procedure

The jet reconstruction procedures closely follow those used by ATLAS for previous jet measurements in Pb+Pb collisions. Jets were reconstructed using the anti-k_t algorithm [29] implemented in the `FastJet` software package [15]. The jets with radius parameter $R = 0.2$ were formed by clustering calorimetric "towers" of spatial size $\Delta\eta \times \Delta\phi = 0.1 \times \frac{\pi}{32}$. The energies in the towers are obtained by summing the energies of calorimeter cells at the electromagnetic energy scale [30] within the tower boundaries. A background subtraction procedure was applied that uses the UE average transverse energy density, $\rho(\eta, \phi)$, where the ϕ dependence is due to global azimuthal correlations in the particle production typically referred to as "flow" [31]. The modulation accounts for the contribution of the second, third, and fourth-order azimuthal anisotropy harmonics characterized by values of flow coefficients v_n. The UE is also corrected for η- and ϕ-dependent non-uniformities of the detector response by multiplicative correction factor derived in MB Pb+Pb data. An iterative procedure was used to remove the impact of jets on ρ and the v_n values. The first estimate of the UE average transverse energy density, $\rho(\eta)$, was evaluated in 0.1 intervals of η excluding those within "seed" jets. In the first step of the iterative subtraction, the seeds are defined to be a conjunction of $R = 0.2$ jets and $R = 0.4$ track jets. Track jets are reconstructed by applying the anti-k_t algorithm with $R = 0.4$ to charged particles with $p_{\mathrm{T}} > 4$ GeV. The $R = 0.2$ jets have to pass a cut on the value of maximal-over-mean tower energy, while the track jets are required to have $p_{\mathrm{T}} > 7$ GeV. The background is then subtracted from each tower constituent, and the jets' kinematics are recalculated.

After the first iteration, the ρ and v_n values are updated by excluding regions within $\Delta R < 0.4$ from the newly reconstructed $R = 0.2$ jets with $p_{\mathrm{T}} > 25$ GeV (8 GeV in pp collisions), and track jets. The updated ρ and v_n values are used to update the jets' kinematics in the second iteration.

Following the subtraction procedure, a jet η- and p_{T}-dependent multiplicative correction factors, derived in the MC simulations, are applied to the jet four-vector to correct for the calorimeter energy response [32]. An additional correction based on *in situ* studies of jets recoiling against photons, Z bosons, and jets in other regions of the calorimeter is applied [33]. This calibration is followed by "cross-calibration" which relates the jet energy scale (JES) of jets reconstructed by the procedure outlined in this section with the JES of jets used in 13 TeV pp collisions [34]. The jet reconstruction in pp collisions is performed using the same procedure as in heavy-ion collisions but without correcting the UE for η and ϕ variation in the detector response and without azimuthal modulation of the UE.

Generator-level jets are built from particle four-vectors obtained from the MC generator. Truth jets are defined by applying the anti-k_t algorithm with radius parameter $R = 0.2$ to stable particles with a proper lifetime greater than 30 ps, but excluding muons and neutrinos, which do not leave significant energy deposits in the calorimeter.

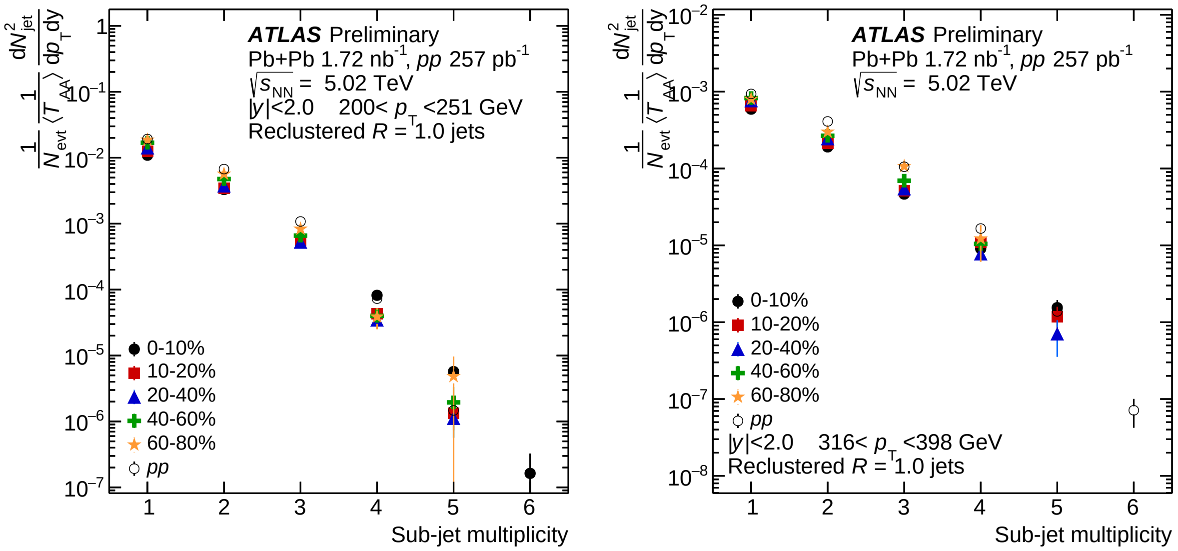

Figure 1: Uncorrected distributions of the number of sub-jets of the large-radius jets in *pp* collisions and five centrality intervals of Pb+Pb collisions for jet with p_T in the range 200–251 GeV (left) and 316–398 GeV (right).

The reconstructed and truth large-radius jets used in this note are built by clustering the reconstructed and truth anti-k_t $R = 0.2$ jets, respectively, with $p_T > 35$ GeV and $|\eta| < 3.0$. The anti-k_t algorithm with distance parameter $R = 1.0$ is used. The resulting jets are referred to as large-radius jets in this note. Reconstructed large-radius jets are matched to large-radius truth jets using the criterion $\Delta R < 0.75$ for performance studies and deriving response matrices used in the unfolding. The k_t clustering of large-radius jet constituents with only single sub-jet results by convention in $\sqrt{d_{12}} = 0$. The intervals $\sqrt{d_{12}}$ used in this analysis are designed in such that the first interval is populated only by large-radius jets with a single sub-jet (“SSJ”).

The measured uncorrected distributions of the number of sub-jets of large-radius jets in *pp* and Pb+Pb collisions for jets with p_T of 200–251 GeV and 316–398 GeV are presented in Figure 1. The yields of large-radius jets sharply decrease with increasing sub-jets multiplicity with the most probable configuration of single sub-jet both in Pb+Pb and *pp* collisions. The centrality dependence shows an overall decrease in the yields of large-radius jets in more central collisions at lower multiplicities and an enhancement at higher multiplicities for lower p_T large-radius jets. The enhancement can be attributed to the contribution of combinatorial jets from independent hard scatterings in one Pb+Pb collision and from jet energy resolution.

Performance of the reconstruction of large-radius jets is characterised by evaluating the JES and jet energy resolution (JER), which correspond to the mean and width of p_T^{reco}/p_T^{truth} distribution, respectively, where p_T^{reco} is the reconstructed large-radius jet p_T and p_T^{truth} is transverse momentum of the matched large-radius truth jet. The JES and JER as a function of p_T^{truth} are shown in Figure 2 . The JES deviates from unity by less than 1% for low-p_T large-radius jets and up to 2% for high-p_T large-radius jets with no significant centrality dependence. Typically in HI collisions, increasing the value of R results in a larger JER as the larger area jet includes more UE. In this case, because the $R = 1.0$ jets are reclustered from $R = 0.2$ jets and have small sub-jet multiplicity, this effect is not very large and the resolution is similar to that of $R = 0.2$ jets [35].

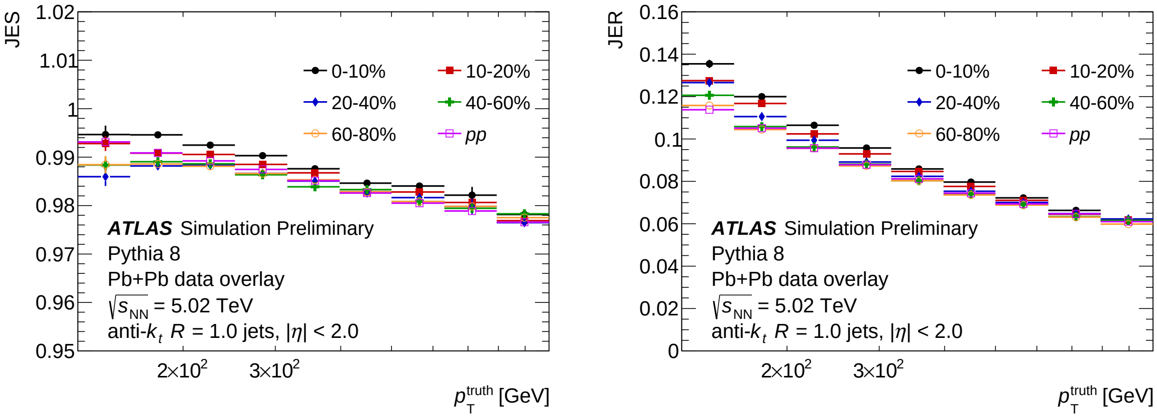

Figure 2: The JES (left) and JER (right) as a function of $p_{\mathrm{T}}^{\mathrm{truth}}$ evaluated in pp and 5 centrality intervals of Pb+Pb MC events for $R = 1.0$ jets within $|y| < 2.0$.

The large-radius jet yields in Pb+Pb collisions and jet cross-section in pp collisions are measured in the rapidity range of $|y| < 2.0$. The $\sqrt{d_{12}}$-inclusive measurement is performed as a function of the large-radius jet p_{T} from 156 GeV to 1 TeV. The measurement as a function of the $\sqrt{d_{12}}$ is presented in coarser p_{T} intervals ranging from 200 GeV to 500 GeV and for $\sqrt{d_{12}}$ values from 0 to 172 GeV.

The measured distributions are fully corrected for detector effects by the unfolding procedure using the iterative Bayesian unfolding method [36] from the `RooUnfold` software package [37]. The unfolding removes the effects of bin migrations due to the jet energy resolution and residual jet energy scale non-closure. The unfolding also corrects for the combinatoric sub-jet contribution resulting in the migration in $\sqrt{d_{12}}$. The yields as a function of $\sqrt{d_{12}}$ are unfolded using a two-dimensional unfolding simultaneously in p_{T} and $\sqrt{d_{12}}$ while the inclusive jet yields are unfolded using a one-dimensional unfolding in p_{T}. The response matrices are built from large-radius reconstructed jets matched to large-radius truth jets. The unmatched truth jets are incorporated as an efficiency correction. No reconstructed-to-truth jet matching requirement is imposed on sub-jets. The response matrices are generated separately for pp collisions and for each centrality interval in Pb+Pb collisions. To better represent the data, the response was re-weighted along the truth-jet axes by the reconstructed level data-to-MC ratio. The number of iterations in the unfolding was chosen so that the result is stable when changing the number of iterations while minimizing the amplification of statistical uncertainties. Four iterations are used to unfold inclusive large-radius yields and six iterations are used in the two-dimensional unfolding of the yields as a function of $\sqrt{d_{12}}$.

5 Systematic uncertainties

The following sources of systematic uncertainty are considered for this analysis: JES, JER, the sensitivity of the unfolding to the prior, the MC statistical uncertainty, the residual non-closure of the analysis procedure, the determination of the mean nuclear thickness function $\langle T_{\mathrm{AA}} \rangle$ values, and the pp luminosity. The uncertainties of JES and JER are applied to small-radius jets and propagated through reclustering to large-radius jets.

The systematic uncertainty on jets due to the JES has five components. First part is a centrality-independent baseline component that is determined from *in situ* studies of the calorimeter response of jets reconstructed with procedure used in 13 TeV pp collisions [38, 39]. The second centrality-independent component accounts for the relative energy scale difference between the jet reconstruction procedures used in this note and that in 13 TeV pp collisions [34]. Potential inaccuracies in the MC sample in the description of the relative abundances of jets initiated by quarks and gluons and of the calorimetric response to quark and gluon jets are accounted for by the third component. The fourth, centrality-dependent, component accounts for a different structure and possibly a different detector response of jets in Pb+Pb collisions that is not modeled by the MC. It is evaluated by the method used for 2015 and 2011 data [34] that compares calorimeter p_{T} and the sum of the transverse momentum of charged particles within the jet in data and MC samples. The size of the centrality-dependent uncertainty on the JES reaches 0.8% in the most central collisions. The systematic uncertainties from JES discussed above are derived for $R = 0.4$ jets. The last component does not depend on collision centrality and it accounts for the potential difference in uncertainties between $R = 0.4$ and $R = 0.2$ jets. Centrality-independent components affect the JES both in pp and Pb+Pb collisions and are correlated between the two colliding systems while the third component is applied only to Pb+Pb collisions. Each component is varied separately by ± 1 standard deviations in MC samples, applied as a function of p_{T} and η, and the response matrix is recomputed. The data are then unfolded with the modified matrices. The resulting uncertainty from the JES on the inclusive jet spectra is at the level of 10% with a small increase with collision centrality and p_{T}. The size of the uncertainty due to the JES is significantly reduced when R_{AA} distributions are evaluated and varies from 3% at low p_{T} to 5% at high p_{T}. The uncertainty on jet yields as a function of $\sqrt{d_{12}}$ is similar to that on inclusive jet spectra except for an increase at the lowest intervals of $\sqrt{d_{12}}$.

The uncertainty due to the JER is evaluated by repeating the unfolding procedure with modified response matrices, where an additional contribution is added to the resolution of the reconstructed $p_{\mathrm{T}}^{\mathrm{jet}}$ using a Gaussian smearing procedure. The smearing factor is evaluated using an *in situ* technique in 13 TeV pp data that involves studies of dijet energy balance [40, 41] with additional contributions accounting for differences in calibration procedures for jets used in this analysis and those from 13 TeV pp data. Further, uncertainty is included to account for differences between the tower-based jet reconstruction and the jet reconstruction used in analyses of 13 TeV pp data. Similarly to the JES, an additional uncertainty on the JER is added to account for differences between $R = 0.2$ and $R = 0.4$ jets. The resulting uncertainty from the JER is symmetrized. The size of the resulting uncertainty due to the JER typically reaches 3% on the inclusive large-radius jet yields, but it reaches up to 20% in the measurement of jet yields as a function of $\sqrt{d_{12}}$ at lowest values of $\sqrt{d_{12}}$ in the central Pb+Pb collisions.

The systematic uncertainty on the unfolding procedure is estimated by repeating the analysis with response matrices without the re-weighting to match the shapes of measured distributions in data. The difference between the nominal distribution and that unfolded with the un-reweighted response matrix is taken as the systematic uncertainty. This results in an uncertainty less than 1% on the inclusive jet spectra and $R_{\mathrm{AA}}(p_{\mathrm{T}})$, but it is up to 20% for $R_{\mathrm{AA}}(\sqrt{d_{12}})$ at the lowest values of $\sqrt{d_{12}}$.

The uncertainty of the mean nuclear thickness function arises from geometric modeling uncertainties (nucleon–nucleon inelastic cross-section, Woods–Saxon parameterization of the nucleon distribution) and the uncertainty of the fraction of selected inelastic Pb+Pb collisions. The values of these uncertainties are taken from Ref. [42]. The integrated luminosity determined for 2017 pp data was calibrated using data from dedicated beam separation scans with the relative systematic uncertainty of 1.6%.

The sensitivity to the statistical limitations of the MC samples is determined through pseudo-experiments by re-sampling entries in the response matrices according to their uncertainty. The resulting uncertainty is smaller than 1% in the inclusive large-radius jet measurement and for low values of $\sqrt{d_{12}}$, and increases to up to 5% for the highest values of $\sqrt{d_{12}}$. Uncertainties arising from statistical fluctuations at the data are evaluated using a similar procedure, by re-sampling the data distributions according to their statistical uncertainties.

An additional uncertainty to account for possible residual limitations in the analysis procedure is assigned by evaluating the non-closure of the unfolded distributions in simulations.

The correlations between the various components of the systematic uncertainty are considered in evaluating the R_{AA}. The uncertainties due to the mean nuclear thickness function, the limitation in MC statistics, pp luminosity, the centrality-dependent component of the JES, and the statistical uncertainty on the data are taken to be uncorrelated between pp and Pb+Pb collisions, while all others are taken to be correlated. The partial cancellation of the resulting systematic uncertainties from correlated sources results in smaller uncertainties on the R_{AA} distributions compared to those on the cross-sections and yields. Systematic uncertainties can be also categorised into two classes based on their point-to-point correlation: bin-wise correlated uncertainties and uncertainties that affect the overall normalisation of distributions. Uncertainties due to the determination of $\langle T_{\mathrm{AA}} \rangle$ and pp luminosity belong to the second class, all other uncertainties belong to the first.

Examples of systematic uncertainties are shown in Figure 3 for the inclusive large-radius jet cross-sections and yields in pp and Pb+Pb collisions, for large-radius jet yields as a function of $\sqrt{d_{12}}$ with p_{T} in the interval of 316–398 GeV, and for R_{AA}. The total uncertainties for cross-sections and yields are dominated by the centrality independent uncertainty from the JES both in pp and Pb+Pb collisions, while the uncertainty for R_{AA} is dominated by the centrality dependent component. Uncertainties on unfolding and JER contribute significantly in low values of $\sqrt{d_{12}}$ in Pb+Pb collisions.

6 Results

The inclusive large-radius jet cross-section in pp collisions and per-event Pb+Pb yields scaled by $\langle T_{\mathrm{AA}} \rangle$ in five centrality intervals are shown in the left panel of Figure 4. The error bars in the figure represent statistical uncertainties while the shaded boxes represent systematic uncertainties. The systematic uncertainties also include the point-to-point correlated uncertainty of the luminosity and $\langle T_{\mathrm{AA}} \rangle$. The jet cross-section and jet yields are presented in a rapidity interval of $|y| < 2.0$ and for large-radius jets with p_{T} between 158 GeV and 1000 GeV.

The nuclear modification factor, R_{AA}, evaluated as a function of jet p_{T} in five centrality intervals is presented in the right panel of Figure 4. A clear suppression of the inclusive large-radius jet production in central Pb+Pb collisions with respect to pp collisions can be seen. In 0-10% central collisions the R_{AA} reaches a value of approximately 0.5 at $p_{\mathrm{T}} = 200$ GeV while growing slowly with increasing jet p_{T}. It stays bellow 0.6 for jets with p_{T} up to 600 GeV. These observations are in qualitative agreement with those reported in a similar measurement performed in Pb+Pb collisions at $\sqrt{s_{\mathrm{NN}}} = 5.02$ TeV for $R = 0.4$ jets [42]. However, the magnitude of the R_{AA} is lower compared to that for $R = 0.4$ jets which reaches a value of 0.6 around 300 GeV. The comparison of R_{AA} for $R = 0.4$ and $R = 1.0$ is presented in Figure 5. Various theoretical calculations of the jet quenching where the jet energy is distributed to soft particles predict a smaller suppression when expanding the jet radius by recovering more lost energy [43, 44]. This is not the case for the re-clustered jets where the energy radiated between $R = 0.2$ sub-jets is removed and lost energy is not recovered.

The inclusive $R = 1.0$ jet cross-section in pp collision data compared with per-event-yields scaled by $\langle T_{\mathrm{AA}} \rangle$ in Pb+Pb collisions as a function of the k_t splitting scale $\sqrt{d_{12}}$ in four intervals of jet p_{T} ranging from

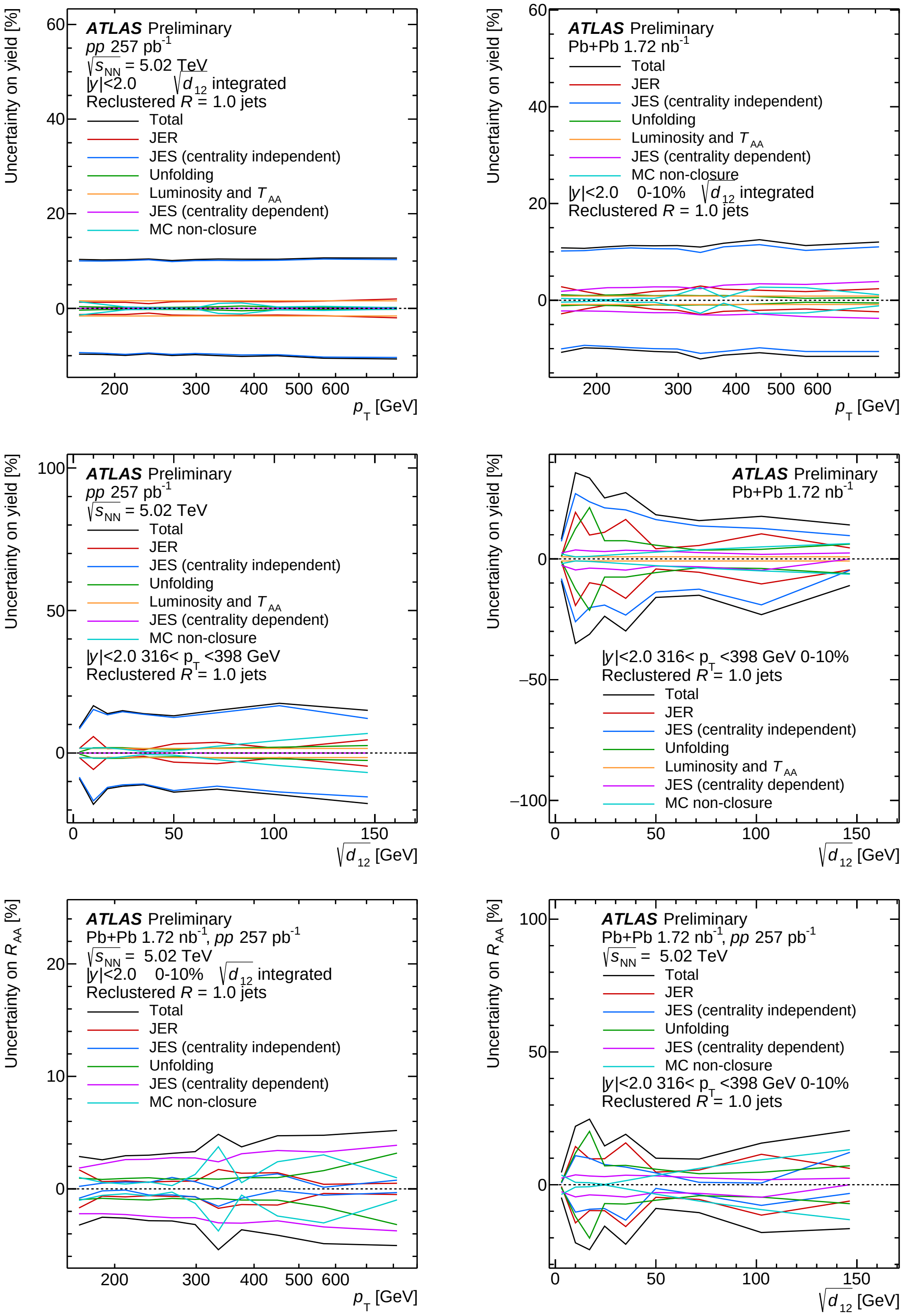

Figure 3: Relative size of the systematic uncertainties for inclusive $R = 1.0$ jet cross-sections and yields in pp (top-left panel) and Pb+Pb collisions (top-right panel), for large-radius jet yields measured as a function of $\sqrt{d_{12}}$ with p_{T} in the range 316–398 GeV in pp and Pb+Pb collisions (middle panels), and for R_{AA} as function of jet p_{T} (bottom-left) and $\sqrt{d_{12}}$ (bottom-right). The systematic uncertainties due to centrality dependent and independent JES, JER, unfolding, MC non-closure, luminosity and $\langle T_{\mathrm{AA}}\rangle$ are shown. Uncertainty on $\langle T_{\mathrm{AA}}\rangle$ and luminosity is shown only for yields, not for R_{AA} ratios. The black line shows the total systematic uncertainty.

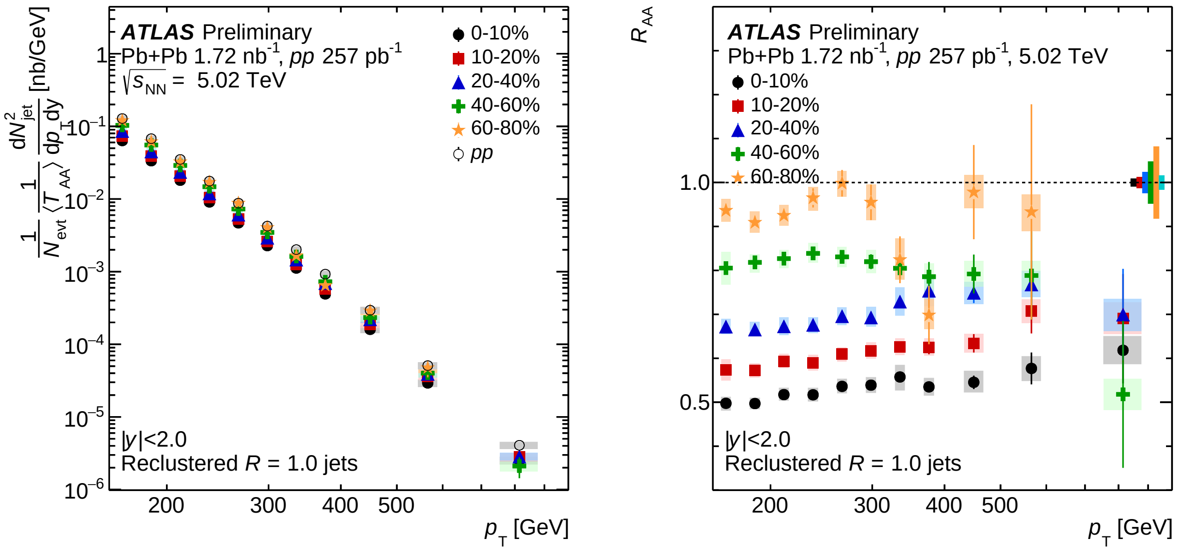

Figure 4: Left: comparison of $\langle T_{\mathrm{AA}} \rangle$ normalized per-event inclusive $R = 1.0$ jet yields in five centrality intervals in Pb+Pb collisions and cross-section in pp collisions. Right: The values of R_{AA} for inclusive $R = 1.0$ jets as function of p_{T} in five centrality intervals. The vertical bars on the data points indicate statistical uncertainties, while the shaded boxes indicate systematic uncertainties. The systematic uncertainties on yields also include the uncertainty due to the luminosity and $\langle T_{\mathrm{AA}} \rangle$, which is correlated for all the data points. The colored boxes at $R_{\mathrm{AA}} = 1$ represent fractional uncertainty on $\langle T_{\mathrm{AA}} \rangle$ and pp luminosity (cyan), which both affect the overall normalisation. The widths of the boxes are not indicative of the bin size.

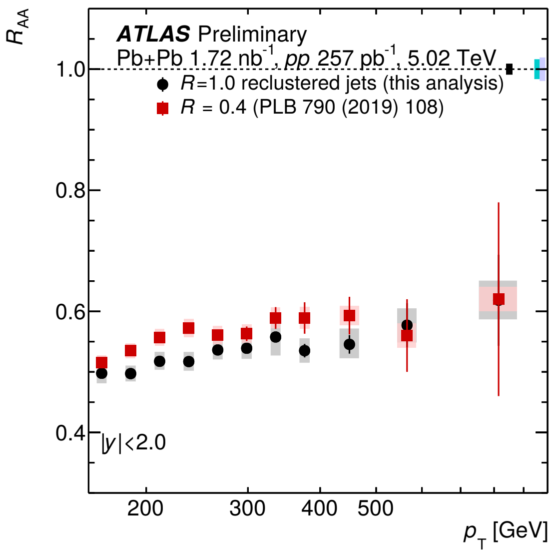

Figure 5: Comparison of R_{AA} for $R = 1.0$ jets as a function of jet p_{T} to the same quantity measured with $R = 0.4$ anti-k_t jets [42] in 0–10% centrality interval. The R_{AA} for $R = 0.4$ is evaluated for jets with $|y| < 2.8$ while this analysis is done for jets with $|y| < 2.0$. The vertical bars on the data points indicate statistical uncertainties, while the shaded boxes indicate systematic uncertainties. The colored boxes at $R_{\mathrm{AA}} = 1$ represent fractional uncertainty on $\langle T_{\mathrm{AA}} \rangle$ (black) and pp luminosity in this measurement (cyan) and pp luminosity in previous analysis [42](light-blue), which both affect the overall normalisation. The widths of the boxes are not indicative of the bin size.

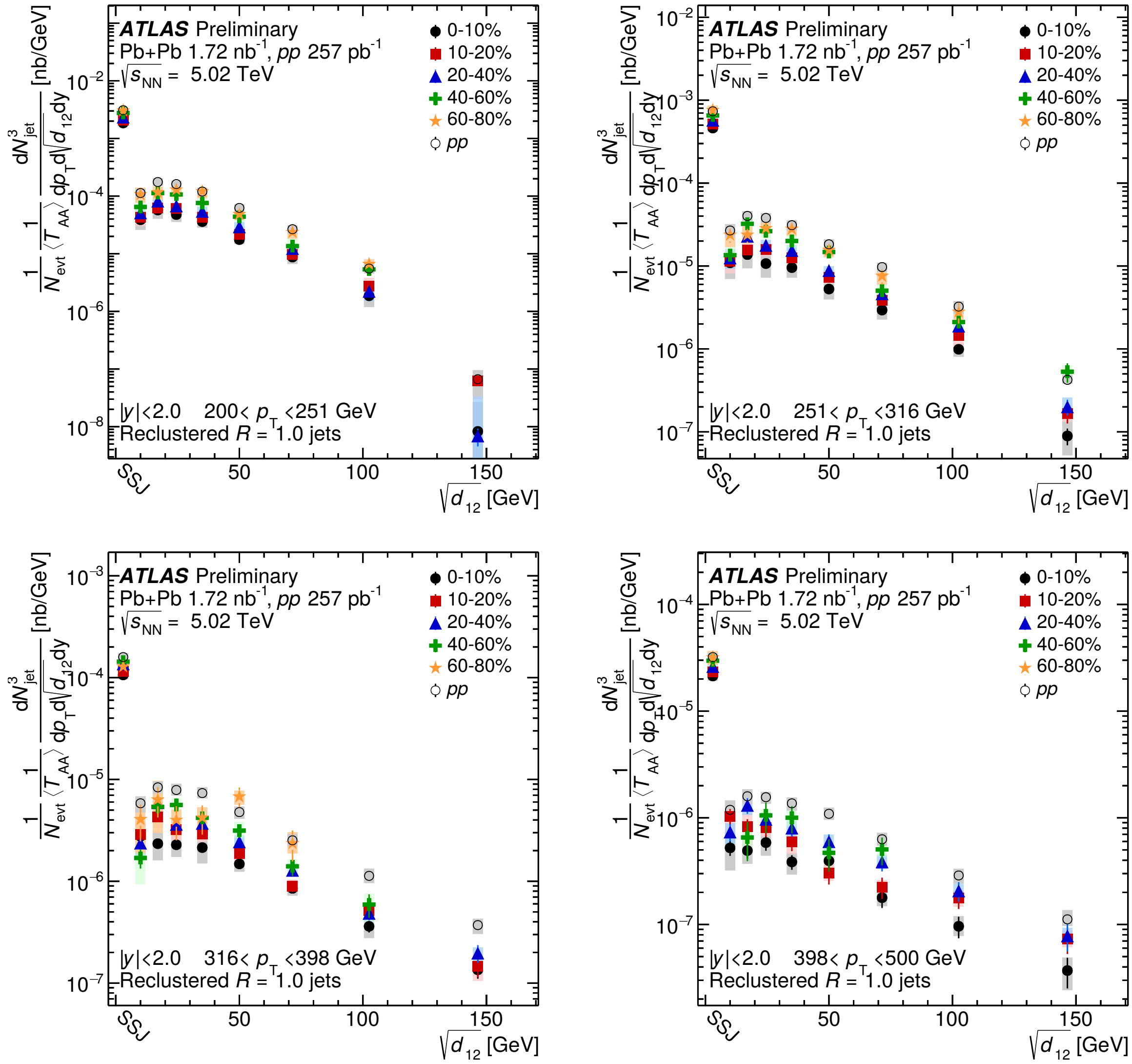

Figure 6: Comparison of $\langle T_{\mathrm{AA}} \rangle$ normalized per-event $R = 1.0$ jet yields as function of k_t splitting scale, $\sqrt{d_{12}}$, in five centrality and four jet p_{T} intervals in Pb+Pb collisions and large-radius jet cross-section in pp collisions. The vertical bars on the data points indicate statistical uncertainties, while the shaded boxes indicate systematic uncertainties. The systematic uncertainties also include the uncertainty due to the luminosity and $\langle T_{\mathrm{AA}} \rangle$, which is correlated for all the data points. The widths of the boxes are not indicative of the bin size. The first interval is populated only by large-radius jets with a single sub-jet and labeled as “SSJ”.

200 GeV to 500 GeV is shown in Figure 6. The per-event $\langle T_{\mathrm{AA}} \rangle$ normalized jet yields in Pb+Pb fall below cross-section in pp collisions, showing the jet suppression in all intervals of $\sqrt{d_{12}}$.

The nuclear modification factor evaluated as a function of the $\sqrt{d_{12}}$ is shown in Figure 7. The R_{AA} values for large-radius jets with a single sub-jets is significantly different compared to the R_{AA} for large-radius jets with more complex substructure with a non-zero $\sqrt{d_{12}}$. The R_{AA} sharply decreases with increasing $\sqrt{d_{12}}$ for small values of the splitting scale followed by flattening for larger $\sqrt{d_{12}}$. This observation is qualitatively consistent with the effects where the medium can not resolve partonic fragments below a

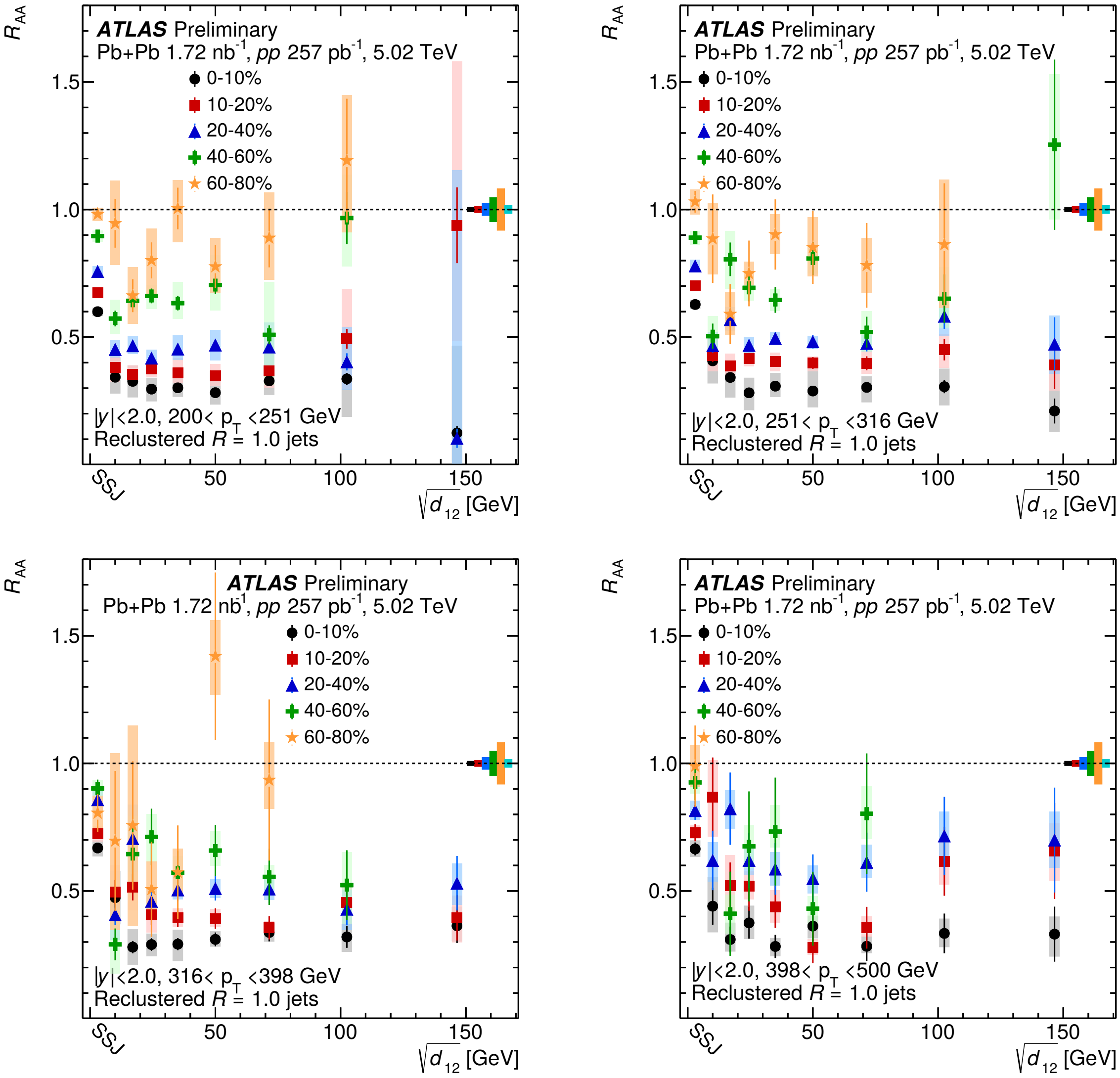

Figure 7: R_{AA} of $R = 1.0$ jet yields as function of k_t splitting scale, $\sqrt{d_{12}}$, in five centrality and four jet p_{T} intervals. The vertical bars on the data points indicate statistical uncertainties, while the shaded boxes indicate systematic uncertainties. The colored boxes at $R_{\mathrm{AA}} = 1$ represent fractional uncertainty on $\langle T_{\mathrm{AA}} \rangle$ and pp luminosity (cyan), which both affect the overall normalisation. The widths of the boxes are not indicative of the bin size. The first interval is populated only by large-radius jets with a single sub-jet and labeled as “SSJ”.

certain transverse scale [10]. However, the magnitude of the suppression is expected to depend no only on the energy loss but also on the shape of the initial jet production p_{T} spectrum. This result is also consistent with the previous measurement of correlated production of pairs of nearby jets in Pb+Pb collisions [5]. The measurement reported suppression of yields of neighboring jets by 30% to 50% in the most central collisions with respect to the pp reference which suggests even larger suppression of per-event yields when the suppression of inclusive jet yields is taken into account.

The nuclear modification factor, evaluated as a function of $\langle N_{\mathrm{part}} \rangle$, is shown in Figure 8 for four jet p_{T} and $\sqrt{d_{12}}$ intervals. The systematic uncertainties on data points include also the uncertainty from the $\langle T_{\mathrm{AA}} \rangle$. A

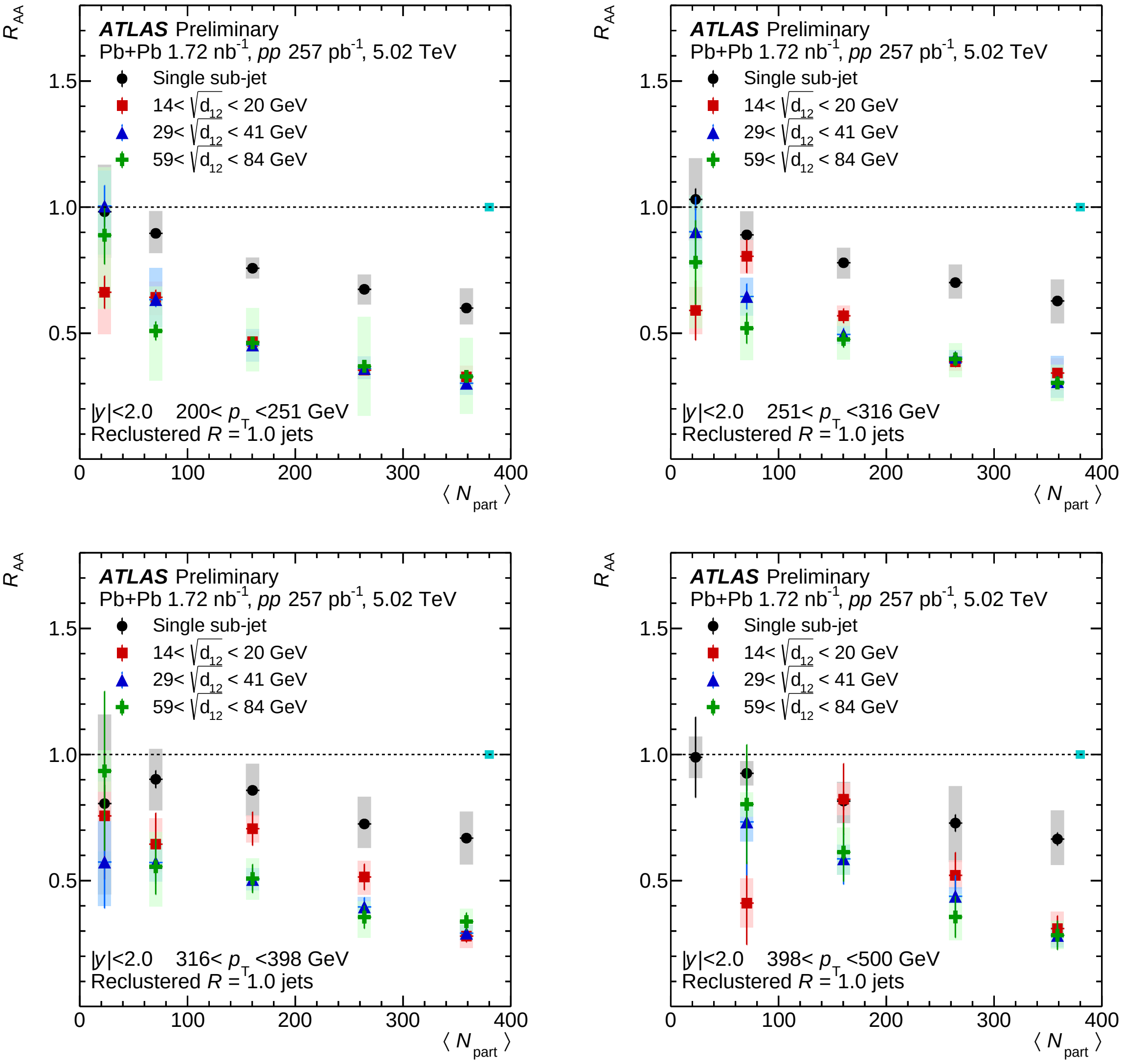

Figure 8: The R_{AA} values evaluated as a function of $\langle N_{\text{part}} \rangle$ for four different $R = 1.0$ jet p_T intervals and different intervals of $\sqrt{d_{12}}$. The vertical bars on the data points indicate statistical uncertainties, while the shaded boxes indicate systematic uncertainties. The systematic uncertainties also include the uncertainty due to the $\langle T_{AA} \rangle$. The cyan box at $R_{AA} = 1$ represents fractional uncertainty on pp luminosity. The widths of the boxes are not indicative of the bin size.

continuous increase of the suppression with increasing centrality is observed. The jets with single sub-jet are less suppressed with respect to those with higher sub-jet multiplicity.

The R_{AA} is also evaluated as a function of p_T in intervals of $\sqrt{d_{12}}$ and presented in Figure 9 for different centrality intervals. For large-radius jets with a single sub-jet, the R_{AA} grows slowly with increasing jet p_T, while no significant p_T dependence is seen for those large-radius jets with multiple sub-jets.

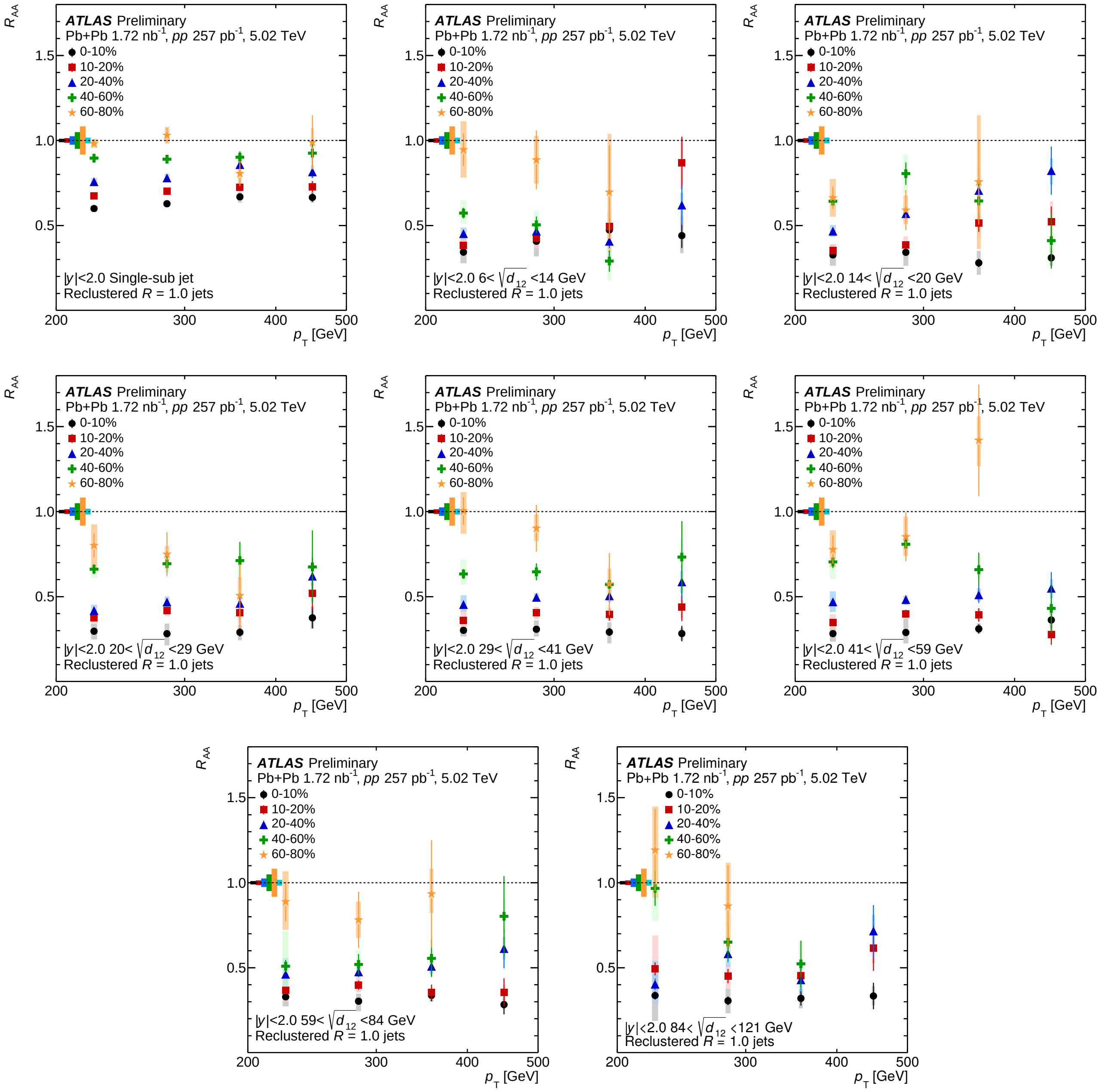

Figure 9: R_{AA} of $R = 1.0$ jet yields as function of jet p_{T} in eight intervals of k_t splitting scale, $\sqrt{d_{12}}$, and five centrality intervals. The vertical bars on the data points indicate statistical uncertainties, while the shaded boxes indicate systematic uncertainties. The colored boxes at $R_{\mathrm{AA}} = 1$ represent fractional uncertainty on $\langle T_{\mathrm{AA}} \rangle$ and pp luminosity (cyan), which both affect the overall normalisation. The widths of the boxes are not indicative of the bin size.

7 Summary and conclusions

This note presents a measurement of the cross-section and per-event yields in pp and Pb+Pb collisions, respectively, of $R = 1.0$ anti-k_t jets reclustered from $R = 0.2$ anti-k_t jets with $p_{\mathrm{T}} > 35$ GeV. The measurement is performed over the rapidity interval $|y| < 2.0$ in five collision centrality intervals and different intervals of $R = 1.0$ jet transverse momenta spanning the range 156–1000 GeV. The results are fully corrected for detector response. The measurement is performed utilizing pp and Pb+Pb data at the nucleon–nucleon center-of-mass energy of $\sqrt{s_{\mathrm{NN}}} = 5.02$ TeV collected by the ATLAS detector at the LHC in 2017 and 2018, respectively. The modification of per-event-yields in Pb+Pb collisions with respect to the reference from pp collisions is evaluated using nuclear modification factor, R_{AA}, where the jet yields measured in heavy-ion collisions are scaled by the mean nuclear thickness function, $\langle T_{\mathrm{AA}} \rangle$. Inclusive per-event $\langle T_{\mathrm{AA}} \rangle$-normalized yields in Pb+Pb collisions are observed to be suppressed with respect to the jet cross-section measured in pp collisions. The magnitude of the R_{AA} monotonically increases from central to peripheral collisions. A small but continuous increase of the R_{AA} with p_{T} is observed in the central Pb+Pb collisions. To further study the medium induced effects during the parton shower evolution, this note reports measurement of the cross-section and per-event yields in intervals of the k_t splitting scale, $\sqrt{d_{12}}$. A significant evolution of R_{AA} with $\sqrt{d_{12}}$ is observed, at small $\sqrt{d_{12}}$ values, indicating a significant difference in the quenching of large-radius jets having single sub-jet and those with more complex substructure. No significant dependence of R_{AA} on $\sqrt{d_{12}}$ is observed at larger $\sqrt{d_{12}}$.

References

[1] M. Gyulassy and L. McLerran, *New forms of QCD matter discovered at RHIC*, Nucl. Phys. A **750** (2005) 30, arXiv: `nucl-th/0405013 [nucl-th]` (cit. on p. 2).

[2] E. Shuryak, *Strongly coupled quark-gluon plasma in heavy ion collisions*, Rev. Mod. Phys. **89** (2017) 035001, arXiv: `1412.8393 [hep-ph]` (cit. on p. 2).

[3] R. Pasechnik and M. Šumbera, *Phenomenological Review on Quark–Gluon Plasma: Concepts vs. Observations*, Universe **3** (2017) 7, arXiv: `1611.01533 [hep-ph]` (cit. on p. 2).

[4] W. Busza, K. Rajagopal and W. van der Schee, *Heavy Ion Collisions: The Big Picture, and the Big Questions*, (2018), arXiv: `1802.04801 [hep-ph]` (cit. on p. 2).

[5] ATLAS Collaboration, *Measurement of the production of neighbouring jets in lead-lead collisions at $\sqrt{s_{NN}} = 2.76$ TeV with the ATLAS detector*, Phys. Lett. B **751** (2015) 376, arXiv: `1506.08656 [hep-ex]` (cit. on pp. 2, 4, 13).

[6] ATLAS collaboration, *Measurement of angular and momentum distributions of charged particles within and around jets in Pb+Pb and pp collisions at $\sqrt{s_{\mathrm{NN}}} = 5.02$ TeV with the ATLAS detector*, (2019), arXiv: `1908.05264 [nucl-ex]` (cit. on p. 2).

[7] CMS Collaboration, *Decomposing transverse momentum balance contributions for quenched jets in PbPb collisions at $\sqrt{s_{\mathrm{NN}}} = 2.76$ TeV*, JHEP **11** (2016) 055, arXiv: `1609.02466 [nucl-ex]` (cit. on p. 2).

[8] Y. Mehtar-Tani and K. Tywoniuk, *Jet (de)coherence in Pb–Pb collisions at the LHC*, Phys. Lett. B **744** (2015) 284, arXiv: `1401.8293 [hep-ph]` (cit. on p. 2).

[9] J. Casalderrey-Solana, Y. Mehtar-Tani, C. A. Salgado and K. Tywoniuk, *New picture of jet quenching dictated by color coherence*, Phys. Lett. B **725** (2013) 357, arXiv: `1210.7765 [hep-ph]` (cit. on p. 2).

[10] J. Casalderrey-Solana, Y. Mehtar-Tani, C. A. Salgado and K. Tywoniuk, *Probing jet decoherence in heavy ion collisions*, Nucl. Phys. A **967** (2017) 564 (cit. on pp. 2, 13).

[11] Y. Mehtar-Tani, C. A. Salgado and K. Tywoniuk, *Jets in QCD Media: From Color Coherence to Decoherence*, Phys. Lett. B **707** (2012) 156, arXiv: `1102.4317 [hep-ph]` (cit. on p. 2).

[12] ATLAS Collaboration, *Measurement of* $R = 0.4$ *jet mass in Pb+Pb and pp collisions at* $\sqrt{s_{NN}} = 5.02$ *TeV with the ATLAS detector*, ATLAS-CONF-2018-014, 2018, URL: `https://cds.cern.ch/record/2319867` (cit. on p. 2).

[13] ALICE collaboration, *First measurement of jet mass in Pb–Pb and p–Pb collisions at the LHC*, Phys. Lett. B **776** (2018) 249, arXiv: `1702.00804 [nucl-ex]` (cit. on p. 2).

[14] CMS collaboration, *Measurement of the Splitting Function in pp and Pb-Pb Collisions at* $\sqrt{s_{\mathrm{NN}}} =$ *5.02 TeV*, Phys. Rev. Lett. **120** (2018) 142302, arXiv: `1708.09429 [nucl-ex]` (cit. on p. 2).

[15] M. Cacciari, G. P. Salam and G. Soyez, *FastJet user manual*, Eur.Phys.J. **C72** (2012) 1896, arXiv: `1111.6097 [hep-ph]` (cit. on pp. 2, 5).

[16] M. L. Miller, K. Reygers, S. J. Sanders and P. Steinberg, *Glauber modeling in high energy nuclear collisions*, Ann.Rev.Nucl.Part.Sci. **57** (2007) 205, arXiv: `nucl-ex/0701025 [nucl-ex]` (cit. on p. 3).

[17] ATLAS Collaboration, *The ATLAS Experiment at the CERN Large Hadron Collider*, JINST **3** (2008) S08003 (cit. on p. 3).

[18] ATLAS Collaboration, *ATLAS Insertable B-Layer Technical Design Report*, ATLAS-TDR-19, 2010, URL: `https://cds.cern.ch/record/1291633` (cit. on p. 3), Addendum: ATLAS-TDR-19-ADD-1, 2012, URL: `https://cds.cern.ch/record/1451888`.

[19] ATLAS Collaboration, (2012), URL: `https://cds.cern.ch/record/1451888` (cit. on p. 3).

[20] ATLAS Collaboration, *Trigger menu in 2018*, ATL-DAQ-PUB-2019-001, 2019, URL: `https://cds.cern.ch/record/2693402` (cit. on p. 4).

[21] ATLAS Collaboration, *Measurement of longitudinal flow decorrelations in Pb+Pb collisions at* $\sqrt{s_{\mathrm{NN}}} = 2.76$ *and 5.02 TeV with the ATLAS detector*, Eur. Phys. J. C **78** (2018) 142, arXiv: `1709.02301 [nucl-ex]` (cit. on p. 4).

[22] T. Sjöstrand et al., *An introduction to PYTHIA 8.2*, Comput. Phys. Commun. **191** (2015) 159, arXiv: `1410.3012 [hep-ph]` (cit. on p. 4).

[23] ATLAS Collaboration, *ATLAS Pythia 8 tunes to 7 TeV data*, ATL-PHYS-PUB-2014-021, 2014, URL: `https://cds.cern.ch/record/1966419` (cit. on p. 4).

[24] R. D. Ball et al., *Parton distributions with LHC data*, Nucl. Phys. B **867** (2013) 244, arXiv: `1207.1303 [hep-ph]` (cit. on p. 4).

[25] ATLAS Collaboration, *Further ATLAS tunes of PYTHIA 6 and Pythia 8*, ATL-PHYS-PUB-2011-014, 2011, URL: `https://cds.cern.ch/record/1400677` (cit. on p. 5).

[26] A. D. Martin, W. J. Stirling, R. S. Thorne and G. Watt, *Parton distributions for the LHC*, Eur. Phys. J. C **63** (2009) 189, arXiv: `0901.0002 [hep-ph]` (cit. on p. 5).

[27] S. Agostinelli et al., *Geant4—a simulation toolkit*, Nucl. Instrum. Meth. A **506** (2003) 250 (cit. on p. 5).

[28] ATLAS Collaboration, *The ATLAS Simulation Infrastructure*, Eur. Phys. J. C **70** (2010) 823, arXiv: `1005.4568 [physics.ins-det]` (cit. on p. 5).

[29] M. Cacciari, G. P. Salam and G. Soyez, *The Anti-k_t jet clustering algorithm*, JHEP **04** (2008) 063, arXiv: `0802.1189 [hep-ph]` (cit. on p. 5).

[30] ATLAS Collaboration, *Jet energy measurement with the ATLAS detector in proton–proton collisions at $\sqrt{s} = 7$ TeV*, Eur. Phys. J. C **73** (2013) 2304, arXiv: `1112.6426 [hep-ex]` (cit. on p. 5).

[31] ATLAS Collaboration, *Measurement of the azimuthal anisotropy of charged particles produced in $\sqrt{s_{NN}} = 5.02$ TeV Pb+Pb collisions with the ATLAS detector*, Eur. Phys. J. C **78** (2018) 997, arXiv: `1808.03951 [hep-ex]` (cit. on p. 5).

[32] ATLAS Collaboration, *Jet energy measurement and its systematic uncertainty in proton-proton collisions at $\sqrt{s} = 7$ TeV with the ATLAS detector*, Eur. Phys. J. C **75** (2015) 17, arXiv: `1406.0076 [hep-ex]` (cit. on p. 5).

[33] ATLAS Collaboration, *Measurement of photon-jet transverse momentum correlations in 5.02 TeV Pb+Pb and pp collisions with ATLAS*, Phys. Lett. B **789** (2019) 167, arXiv: `1809.07280 [hep-ex]` (cit. on p. 5).

[34] ATLAS Collaboration, *Jet energy scale and its uncertainty for jets reconstructed using the ATLAS heavy ion jet algorithm*, ATLAS-CONF-2015-016, 2015, url: `https://cds.cern.ch/record/2008677` (cit. on pp. 5, 8).

[35] ATLAS Collaboration, *Measurement of the jet radius and transverse momentum dependence of inclusive jet suppression in lead–lead collisions at $\sqrt{s_{NN}} = 2.76$ TeV with the ATLAS detector*, Phys. Lett. B **719** (2013) 220, arXiv: `1208.1967 [hep-ex]` (cit. on p. 6).

[36] G. D'Agostini, *A multidimensional unfolding method based on Bayes' theorem*, Nucl. Instrum. Meth. A **362** (1995) 487 (cit. on p. 7).

[37] T. Adye, *Unfolding algorithms and tests using RooUnfold*, 2011, arXiv: `1105.1160 [physics.data-an]` (cit. on p. 7).

[38] ATLAS Collaboration, *Jet energy measurement with the ATLAS detector in proton-proton collisions at $\sqrt{s} = 7$ TeV*, Eur. Phys. J. C **73** (2013) 2304, arXiv: `1112.6426 [hep-ex]` (cit. on p. 8).

[39] ATLAS Collaboration, *Jet energy scale measurements and their systematic uncertainties in proton-proton collisions at $\sqrt{s} = 13$ TeV with the ATLAS detector*, Phys. Rev. D **96** (2017) 072002, arXiv: `1703.09665 [hep-ex]` (cit. on p. 8).

[40] ATLAS Collaboration, *Jet energy resolution in proton-proton collisions at $\sqrt{s} = 7$ TeV recorded in 2010 with the ATLAS detector*, Eur. Phys. J. C **73** (2013) 2306, arXiv: `1210.6210 [hep-ex]` (cit. on p. 8).

[41] ATLAS Collaboration, *Data-driven determination of the energy scale and resolution of jets reconstructed in the ATLAS calorimeters using dijet and multijet events at $\sqrt{s} = 8$ TeV*, ATLAS-CONF-2015-017, 2015, url: `https://cds.cern.ch/record/2008678` (cit. on p. 8).

[42] ATLAS collaboration, *Measurement of the nuclear modification factor for inclusive jets in Pb+Pb collisions at $\sqrt{s_{\mathrm{NN}}} = 5.02$ TeV with the ATLAS detector*, Phys. Lett. B **790** (2019) 108, arXiv: `1805.05635 [nucl-ex]` (cit. on pp. 8, 9, 11).

[43] Y.-T. Chien and I. Vitev, *Towards the understanding of jet shapes and cross sections in heavy ion collisions using soft-collinear effective theory*, JHEP **05** (2016) 023, arXiv: `1509.07257 [hep-ph]` (cit. on p. 9).

[44] ATLAS collaboration, *Measurement of the jet radius and transverse momentum dependence of inclusive jet suppression in lead-lead collisions at* $\sqrt{s_{NN}} = 2.76$ *TeV with the ATLAS detector*, Phys. Lett. B **719** (2013) 220, arXiv: `1208.1967 [hep-ex]` (cit. on p. 9).